IOP Publishing Journal of Neural Engineering
J. Neural Eng. **11** (2014) 036002 (19pp) doi:10.1088/1741-2560/11/3/036002

The value and cost of complexity in predictive modelling: role of tissue anisotropic conductivity and fibre tracts in neuromodulation

Syed Salman Shahid[1,2], **Marom Bikson**[3], **Humaira Salman**[1], **Peng Wen**[2] **and Tony Ahfock**[2]

[1] Research Center for Modeling and Simulation, National University of Sciences and Technology, Islamabad, Pakistan
[2] School of Mechanical and Electrical Engineering, University of Southern Queensland, Toowoomba, QLD, Australia
[3] Department of Biomedical Engineering, The City College of New York of CUNY, New York, NY, USA

E-mail: salman_cae@hotmail.com

Received 2 July 2013, revised 17 February 2014
Accepted for publication 20 February 2014
Published 16 April 2014

Abstract

Objectives. Computational methods are increasingly used to optimize transcranial direct current stimulation (tDCS) dose strategies and yet complexities of existing approaches limit their clinical access. Since predictive modelling indicates the relevance of subject/pathology based data and hence the need for subject specific modelling, the incremental clinical value of increasingly complex modelling methods must be balanced against the computational and clinical time and costs. For example, the incorporation of multiple tissue layers and measured diffusion tensor (DTI) based conductivity estimates increase model precision but at the cost of clinical and computational resources. Costs related to such complexities aggregate when considering individual optimization and the myriad of potential montages. Here, rather than considering if additional details change current-flow prediction, we consider when added complexities influence clinical decisions. *Approach*. Towards developing quantitative and qualitative metrics of value/cost associated with computational model complexity, we considered field distributions generated by two 4×1 high-definition montages (m1 $= 4 \times 1$ HD montage with anode at C3 and m2 $= 4 \times 1$ HD montage with anode at C1) and a single conventional (m3 = C3-Fp2) tDCS electrode montage. We evaluated statistical methods, including residual error (RE) and relative difference measure (RDM), to consider the clinical impact and utility of increased complexities, namely the influence of skull, muscle and brain anisotropic conductivities in a volume conductor model. *Main results*. Anisotropy modulated current-flow in a montage and region dependent manner. However, significant statistical changes, produced within montage by anisotropy, did not change qualitative peak and topographic comparisons across montages. Thus for the examples analysed, clinical decision on which dose to select would not be altered by the omission of anisotropic brain conductivity. *Significance*. Results illustrate the need to rationally balance the role of model complexity, such as anisotropy in detailed current flow analysis versus value in clinical dose design. However, when extending our analysis to include axonal polarization, the results provide presumably clinically meaningful information. Hence the importance of model complexity may be more relevant with cellular level predictions of neuromodulation.

Keywords: tDCS, brain stimulation, neuronavigation

S Online supplementary data available from stacks.iop.org/JNE/11/036002/mmedia

(Some figures may appear in colour only in the online journal)

1. Introduction

Transcranial direct current stimulation (tDCS) is a non-invasive and painless procedure to regulate cortical excitability. tDCS has been investigated quite extensively for potential therapeutic use in neuro-rehabilitation, depression, chronic pain, focal epilepsy, electroanalgesia, stroke, Alzheimer disease and tinnitus (Boggio *et al* 2007, 2009, Ferrucci *et al* 2008, 2009, Fregni *et* 2006a, 2006b, 2006c, 2007, Fregni and Pascual-Leone 2007, Mignon *et al* 1996, Nitsche *et al* 2009, Schlaug *et al* 2008, Vanneste *et al* 2010, Webster *et al* 2006, Williams *et al* 2009). tDCS is optimized for each indication by controlled tDCS dose, such as the number, shape and strength of injected current through the stimulating electrodes. With the recognition that tDCS dosage design is not trivial (that electrodes cannot simply be placed over a target), computational models are increasingly leveraged in the clinical settings (Antal *et al* 2012, Borckardt *et al* 2012, Dasilva *et al* 2012, Minhas *et al* 2010, Parazzini *et al* 2012a).

Increasingly detailed computational approaches have been proposed in recent years of varying anatomical and physiological details (Hyun Sang *et al* 2009, 2010, Lee *et al* 2009, Oostendorp *et al* 2008, Parazzini *et al* 2011, 2012a). At the same time, computational models predict subject specific variability in susceptibility to the same dose (Datta 2012, Shahid *et al* 2013), indicating the value of individualized modelling, or at least modelling across a set of archetypes. Real translational utility must therefore balance the value of increased sophistication with the cost associated with clinical scanning, computational time and human resources/intervention (e.g. manual correction/pre and post-processing etc). Thus, the question is not 'if different models will yield different predictions', but rather does increased complexity change model predictions in a way that is clinically meaningful and will influence clinical decisions in study design. While this is a complex and application specific question, the first step towards systematizing value, across a myriad of modelling approaches, is to develop a metric of change versus a simpler approach, and then apply a threshold to base on the perceived clinical value and added cost versus the simpler approach. Here, we contrast two general approaches: (1) generic quantification of the intra-montage analysis due to the influence of model complexity (anisotropy) on field distribution, and (2) inter-montage comparison based on the influence of model complexity using qualitative scoring across the montages.

A further hurdle to the application of computational models in clinical design is that models of tDCS only provide the spatial distribution of E/J in a volume conductor. These scalar maps are not adequate to decipher the current flow and neural membrane polarization, which is the first step towards predicting neuromodulation. Efforts have been limited to indicating directional current flow at the grey matter surface based on the polarization of cortical pyramidal neuron somata (Radman *et al* 2009). Here, we address the quantification of fibre bundle polarization. Several factors at the animal, modelling and clinical level suggest that consideration of fibre tract (axon) polarization during tDCS is warranted.

Bikson *et al* (2004) reported the modulatory effect of the weak electric field on the synaptic function with both somatic and axon-terminal mediated effects. Kabakov *et al* (2012) reported the significance of axonal afferent pathway orientation in determining the effects (excitatory or inhibitory) of tDCS. Axonal projections were reported to determine the direction of modulation, with dendritic orientation affecting mostly the magnitude of excitation. Building on decades of stimulation models, Miranda *et al* (2007) predicted that for transcranial magnetic and electric stimulation, the component of the induced electric field parallel to the fibre pathway ($\boldsymbol{E_P}$) predicts likely sites and strength of excitation of fibre tracts.

In this study, a high-resolution anatomically accurate finite element head model with 20 anatomically distinct regions was employed. The assessment was carried out under the influence of directional conductivity of skull, muscles of mastication, eye muscles and brain. Three electrode montages (two HD-tDCS and one conventional tDCS) were used to estimate the spatial distribution of the induced E-field in the head model. The specific head model, electrode montages and the regions of interest were simply exemplary, with the goals of illustrating the divergence between statistical and clinical criteria. The intra-montage differences in E-field patterns were quantified on the basis of the magnitude and distribution variations. Residual error (RE) and relative difference measures (RDM) (Meijs *et al* 2002) were employed to estimate these variations under three considered montages (see appendix A for additional details on these statistical indices). Using qualitative ranking, the role of anisotropic conductivity with inter-montage variation was assessed by comparing the strength of modulation across three regions of interest (ROI). These regions include M1, contralateral M1 and bi-hemispheric supplementary motor area (SMA). Fibre architectures of five ROI were used to investigate the orientation specificity of aforementioned tDCS montages. Fibre tractography provided additional information to understand the role of fibre pathways (neuronavigation) in regulating neural activities.

2. Methodology

2.1. Head model construction

Three scalar MRI volumes consisting of T1, T2 and proton diffusion (PD) weighted MRI datasets were obtained from a publically available dataset, the BrainWeb (Cocosco *et al*

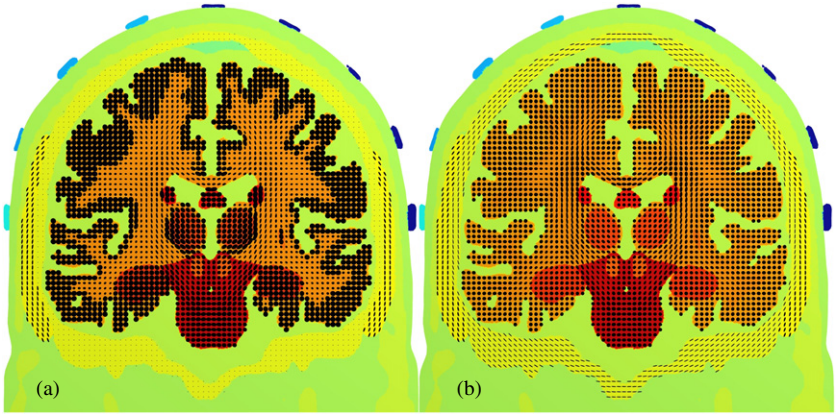

Figure 1. Posterior view of an arbitrary coronal slice, illustrating the anisotropic conductivity distribution in the form of conductivity ellipsoids, (a) non-normalized, (b) normalized. In (a) and (b), electrode locations are marked on the scalp using the International 10-10 EEG electrode system. Skull electrical conductivity being the lowest in the head model makes the skull tensors too small to be properly visible in (a); therefore, (b) has been used to show the same conductivity distribution in a normalized form.

1997). The head models were constructed using the protocols described in our previous study (Shahid *et al* 2014). Two montage categories, classical (C3-Fp2) and HD-tDCS, were considered and electrode configurations corresponding to individual categories were modelled in the ScanCAD (Simpleware, Exeter, UK). The electrode locations were derived from the International 10-10 EEG electrode system. In total, 20 anatomical regions were classified and the baseline model, m1, consisted of around 2 million tetrahedral elements. In order to achieve greater accuracy, the mesh generation algorithm in ScanIP (Simpleware, Exeter, UK) was fine-tuned to obtain higher mesh density in the GM, WM and sub-cortical regions.

The International Consortium of Brain Mapping (ICBM) DTI atlas (ICBM-DTI-81) was used to obtain the co-registered fractional anisotropy (FA), principal diffusion direction and diffusion tensor maps. The methods and the tools used to process the DTI data (averaged and subject-specific) are described elsewhere (Shahid *et al* 2013, 2014). Tissue classification, three-dimensional head model generation, tetrahedral mesh generation and DTI data processing were performed on a Dell T5500 workstation with 24 GB of RAM and 2.0 GHz Xenon processor. Tissue segmentation was performed in a semi-automated manner and took almost 18 h. Three-dimensional head model and tetrahedral mesh were generated in ScanIP in 6 h.

For a real positive definite symmetric tensor, the eigenvalues are always real (positive and non-zero) and the eigenvectors are orthogonal to each other. Under the assumption that in DTI the water self-diffusion is characterized by a multivariate Gaussian distribution, the diffusion tensor can be considered as a covariance matrix describing the translational displacement of diffusing molecules. Therefore, the diffusion tensor can be represented by an ellipsoid highlighting the probabilistic nature of molecular diffusion at a voxel scale (Shimony *et al* 1999, Le Bihan *et al* 2001). The axes (shape) of diffusivity/conductivity ellipsoid can be defined by the three eigenvalues and its orientation (three principal axes) by the corresponding principal eigenvector. Hence, the strength of a conductivity tensor is represented by its principal eigenvalue and its orientation by the corresponding eigenvector. Using an arbitrary coronal slice, figure 1 illustrates the ellipsoidal representation of the conductivity tensor profile. It can be seen that the volumes of WM ellipsoids are variable and smaller than that of the GM and sub-cortical structures (figure 1(a)). This behaviour is indicative of the role of average isotropic conductivity (σ_{ISO}) values used in equation (8).

2.2. Conductivity assignment

The application of quasi-static approximation of Maxwell's equation in a low frequency range (0–10 kHz) is well documented (Plonsey and Heppner 1967, Malmivuo and Plonsey 1995, Nunez and Srinivasan 2006). In this low frequency range, the dominant dielectric behaviour of biological material is only associated with its resistive properties. Under quasi-static assumption, the electric field inside a volume conductor model can be estimated by

$$E = -\nabla V, \tag{1}$$

where V is the potential difference and using Ohm's law, the current density (J) associated with E can be obtained by

$$J = \sigma E, \tag{2}$$

where σ is the electrical conductivity of a medium and for electrically anisotropic materials such as skull, muscle or brain, the conductivity can be represented by a symmetric 3×3 tensor:

$$\sigma = \begin{pmatrix} \sigma_{xx} & \sigma_{xy} & \sigma_{xz} \\ \sigma_{xy} & \sigma_{yy} & \sigma_{yz} \\ \sigma_{xz} & \sigma_{yz} & \sigma_{zz} \end{pmatrix}. \tag{3}$$

In this study, each segmented region of the head model was assigned with their respective average isotropic electrical conductivities. These average values are listed in table 1. In electrical terms, human skull can be considered as a series connection of high, low and high resistor network, respectively. This series network exhibits low conductivity in the radial direction (σ_R) and much higher conductivity in its tangential direction (σ_T) (Wolters *et al* 2006). To represent the directional conductivity of a skull, the conductivity ratio of 10:1 ($\sigma_T =$

Table 1. Isotropic conductivity assignment.

Materials	Conductivity (S m^{-1})	Reference
Scalp	0.43	Holdefer *et al* (2006)
CSF	1.79	Baumann *et al* (1997)
Subcutaneous fat	0.025	Gabriel *et al* (1996a)
Eye-muscles/muscles of mastication	0.16	Gabriel *et al* (1996a)
Eye	0.5	Gabriel *et al* (1996a)
Eye-lens	0.31	Gabriel *et al* (1996b)
Skull	0.015	Oostendorp *et al* (2002)
GM	0.32	Goncalve *et al* (2003)
WM	0.15	Nicholson (1965)
Hindbrain (cerebellum, pons, medulla, brainstem)	0.25	Average brain conductivity (Geddes and Baker 1967)
Red nucleus	0.25	Average brain conductivity (Geddes and Baker 1967)
Thalamus	0.32	Goncalve *et al* (2003)
Hippocampus	0.32	Goncalve *et al* (2003)
Fornix crura	0.32	Goncalve *et al* (2003)
Caudate nucleus	0.32	Goncalve *et al* (2003)
Globus pallidus par externa	0.32	Goncalve *et al* (2003)
Globus pallidus par interna	0.32	Goncalve *et al* (2003)
Putamen	0.32	Goncalve *et al* (2003)
Superior sagittal sinus	1.79	Conductivity of CSF (Baumann *et al* 1997)
Electrode pads	1.4	Datta *et al* (2009)
Conductive gel	0.43	Conductivity of scalp

$10\sigma_R$) was used in this study (Akhtari *et al* 2002, De Munck 1988, Rush and Driscoll 1968).

In order to restrict the volume of a conductivity tensor to its isotropic value (volume), the volume constraint (Wolters 2003) was applied:

$$\tfrac{4}{3}\pi\sigma_R\sigma_T\sigma_T = \tfrac{4}{3}\pi\sigma^3_{\mathrm{ISO}_{\mathrm{SKULL}}}, \tag{4}$$

where $(\sigma_{\mathrm{ISO}_{\mathrm{SKULL}}})$ is the isotropic electrical conductivity of the skull. The tensor representation of the local anisotropic skull conductivity $(\sigma_{\mathrm{ANISO}_{\mathrm{SKULL(local)}}})$ is given by

$$\sigma_{\mathrm{ANISO}_{\mathrm{SKULL(local)}}} = \begin{bmatrix} \sigma_R & & \\ & \sigma_T & \\ & & \sigma_T \end{bmatrix}. \tag{5}$$

The conductivity tensor representation $(\sigma_{\mathrm{ANISO}_{\mathrm{SKULL}}})$ in the Cartesian coordinate system is obtained by the following transformation (eigenvalue decomposition):

$$\sigma_{\mathrm{ANISO}_{\mathrm{SKULL}}} = A\sigma_{\mathrm{ANISO}_{\mathrm{SKULL(local)}}}A^T, \tag{6}$$

where A is the rotational transfer matrix. A custom-built code was written in Matlab script to implement eigenvalue decomposition in COMSOL environment.

Using the same methodology, directional conductivities were introduced in the muscles of mastication $(\sigma_{\mathrm{ANISO}_{\mathrm{muscle}}})$ and eye muscles $(\sigma_{\mathrm{ANISO}_{\mathrm{eye}}})$. However, the longitudinal eigenvalues (σ_L) were chosen to be five times higher than their respective transverse eigenvalues (σ_{Trans}), i.e. $\sigma_L = 5\sigma_{\mathrm{Trans}}$ (Wang *et al* 2001):

$$\sigma_{\mathrm{ANISO}_{\mathrm{muscle}}} = A\begin{bmatrix} \sigma_L & & \\ & \sigma_{\mathrm{Trans}} & \\ & & \sigma_{\mathrm{Trans}} \end{bmatrix}A^T. \tag{7}$$

In this study, the conductivities of the GM, WM and sub-cortical structures were considered anisotropic and the conductivity distribution was estimated from the measured DTI data. The linear conductivity to diffusivity relationship based on the effective medium approach (Tuch *et al* 1999) is not well correlated at the intra-tissue level, although a well-defined linearity was analysed on the intra-tissue level (Kim *et al* 2001). Additionally, the effective medium approach is highly susceptible to the partial volume effect (PVE) of the DT-MRI and may yield unrealistic estimates of conductivity for voxels adulterated with the PVE (Kun *et al* 2008). The derivative of the effective medium algorithm (Hallez *et al* 2008, 2009) uses the volume constraint (Wolters *et al* 2006) to restrict the geometric mean of the eigenvalues, i.e., it keeps the volume of the conductivity tensor equivalent to the volume of the corresponding isotropic tensor. These methods employ the principal eigenvalue and its associated eigenvector to estimate the conductivity profile. A recent study by Shahid *et al* (2013) demonstrated the implications of considering various anisotropic approaches in the forward solution of tDCS. Based on that study, the equivalent isotropic trace algorithm (Miranda *et al* 2001) was selected. This algorithm utilizes the entire diffusion tensor information to define the conductivity distribution and relates the conductivity tensor (σ) to the measured diffusion tensor (D) by a scaling factor, which in turn is based on the ratio of a given isotropic conductivity trace ($3\sigma_{\mathrm{ISO}}$) to the diffusion tensor trace ($D_{xx} + D_{yy} + D_{zz}$):

$$\sigma = \frac{3\sigma_{\mathrm{ISO}}}{\mathrm{trace}(D)}D. \tag{8}$$

The equivalent isotropic trace algorithm was implemented in Matlab and the resulting six conductivity components were exported to COMSOL. This approach estimates the anisotropic conductivity distribution based on the inherent variability in the measured diffusion tensor and at the same time constrains the trace of the conductivity tensor by its equivalent isotropic trace. Since this method keeps the sum of eigenvalues constant (locally), it is not prone to the errors associated with the PVE. Additionally, the use of complete diffusion tensor information, rather than the main eigenvector, has been demonstrated to generate much smoother fibre tract reconstruction along with improvement in fibre propagation in regions of low anisotropy, such as the GM and fibre crossing regions of the WM (Lazar and Alexander 2003, Tensaouti *et al* 2009).

2.3. Electrode configurations and field calculations

In this study, three electrode configurations were assessed based on their efficacy to modulate the selected ROIs. Montage m1 was based on high definition (five electrodes) configuration (Datta *et al* 2009). The location C3 was selected for anode, whereas C1, FC3, CP3 and C5 were considered as cathodes. In montage m2, anode was placed at C1, whereas cathodes were placed at Cz, C3, FC1 and CP1 (figures 3(a) and (b)). Each high-definition electrode had a radius of 6 mm and the conductivity of copper. The electrode gel with the conductivity of 0.43 S m^{-1}, approximate thickness of 2 mm and a radius of 6 mm was emplaced between the scalp and the electrodes. In the third montage m3, 5 $\times$ 5 cm^2 electrode

pads of conductivity 1.4 S m^{-1} were placed at the approximate locations of C3 (anode) and Fp2 (cathode).

Assuming that the spongy pads and gel had their exposed surfaces connected to a constant current stimulator by conductive rubber and copper electrodes, respectively, in such a case, the conductivity of the conductive surfaces can be considered much higher than that of the volume conductor, spongy pads or conductive gel. Therefore, the Dirichlet boundary condition ($V = V_0$) at the exposed surface of the spongy electrode (anode) and conductive gel (anode) and $V = 0$ at the exposed surface of the spongy cathode and the gel can be applied. Remaining external boundaries were considered electrically insulated ($n \cdot J = 0$) and the continuity of the normal component of J was maintained across all the inner boundaries ($n \cdot J_1 = n \cdot J_2$).

In clinical practice, a constant current stimulator is used; therefore, to achieve the desired electric current (1 mA) through the anodes (in all three cases), the voltage across the anode surface was readjusted. Based on the initial estimate ($V = 1$ V), the voltage was readjusted and in order to confirm the injection current of 1 mA through the active surface, the integral of J was determined under each electrode (see appendix B for the list of voltages applied in different simulations to adjust the injected current at 1 mA). The difference between the injected and return currents was estimated to be around 7% in m1 and m2 and 5% in m3. It was observed that this error could further be reduced by using higher order basis functions (Marin *et al* 1998) or selectively increasing the mesh density in specific regions, such as electrodes, gel and scalp. However, further refinement was deemed unnecessary to keep computational cost manageable.

In each case, the resistances between electrodes and current distribution from anodes to cathodes were estimated. Further details shall be discussed in the results and discussion sections. The models considered in this study were electrically passive, i.e. there were no active sources inside the volume conductor. Additionally, the impact of the initial electrical state of neurons on the induced electric field was not considered. However, the effects of the brain fibre architecture were incorporated. Under the quasi-static approximation, Laplace's equation was used to solve the models in a commercial finite element package COMSOL using the algebraic multigrid preconditioned conjugate gradient (AMG_CG) solver setting. The numerical calculations were performed on Dell T7500 workstation, with 24 GB of RAM and two physical Xenon 2.66 GHz processors. For isotropic models, the convergence (error tolerance of 10^{-8}) was achieved in approximately 50 min, whereas, for anisotropic models, 5 extra minutes were required to achieve the desired tolerance.

2.4. Induced E-field tracking and assessment of stimulation mechanism along fibre pathways

The fibre architecture can be used to investigate the orientation specificity of different tDCS montages. With the help of this additional information, it is possible to analyse the role of fibre pathways in regulating the neural activity. Based on the study conducted by Miranda *et al* (2007), three possible neural modulation mechanisms were investigated.

For a long unmyelinated fibre, the passive response of an axon to the induced E-field can be obtained from the Cable equation (Basser and Roth 1990, 1991):

$$\lambda^2 \frac{\partial^2 V}{\partial l^2} - \tau \frac{\partial V}{\partial t} - V = \lambda^2 \frac{\partial E_P}{\partial l}, \tag{9}$$

where τ is the time constant and λ is the space constant. In this study, the value of λ is considered 1 mm (Silva *et al* 2008). At a steady state, change in the membrane potential $V = (V_{\text{membrane}} - V_{\text{resting}})$ due to a sub-threshold stimulus is given by

$$V(l) = -\lambda^2 \frac{\partial E_P}{\partial l}. \tag{10}$$

$\boldsymbol{E_P}$ is the component of the induced electric field ($\boldsymbol{E}$) which is locally parallel to the fibre segment (Δl) having a total length l (mm). In other words, it is the gradient of $\boldsymbol{E_P}$, which defines the potential sites of modulation along a fibre path. Another possible candidate for neural modulation is $\lambda \boldsymbol{E_P}$ itself. For instance, in a high E-field region, for a fibre of length $l \gg \lambda$, a possible site for hyper-/de-polarization would be in the vicinity of fibre termination or a sharp bend. Another possible scenario would involve axons crossing internal boundaries, such as the GM–WM boundary or WM–sub-cortical boundary. Change in tissue conductivity would give rise to a discontinuity in the normal component of the induced E-field. This discontinuity caused by the tissue heterogeneity can lead to a change in the membrane potential:

$$V(l) = -\lambda \frac{\Delta E_P}{2} e^{-\frac{|l|}{\lambda}}. \tag{11}$$

In this study, these mechanisms of neural modulation were compared on fibres of five different regions, namely left cortico-spinal tract (L-CST), right cortico-spinal tract (R-CST), genu of corpus callosum (G-CC), splenium of corpus callosum (S-CC), middle section of corpus callosum (M-CC) and modified fibres of L-CST.

These fibres were generated by the orientation corrected and co-registered principal eigenvectors and the *FA* maps. Using the regions of interest as proposed by Wakana *et al* (2007), these parameters were used to perform the fibre tracking using the deterministic approach, FACT (fibre assignment by continuous tracking), implemented in the DTI studio (Jiang *et al* 2006). Five ROIs were created to perform the fibre tracking with the *FA* threshold of 0.2 and the angle limit of 45°. As a special case, selected fibres across L-CST were tracked using the *FA* threshold of 0.1 and the angle limit of 75°. The motive behind this was to analyse the role of fibre crossing at the GM–WM interface along with the impact of sharp bends on membrane de-/hyper-polarization. Using a custom-built code in Matlab, artificial bends were introduced by assuming that these fibres tend to be projected normal to the local WM boundary. To ensure smooth transition along the fibre path, spline interpolation was applied. Fibres were assigned their respective $\boldsymbol{E_P}$ values using the cubic interpolation. The activating functions, equations (10) and (11), were implemented, along the stretches of the fibres, using a custom-built code in Matlab and 3D visualization was performed in the Paraview (Squillacote 2007).

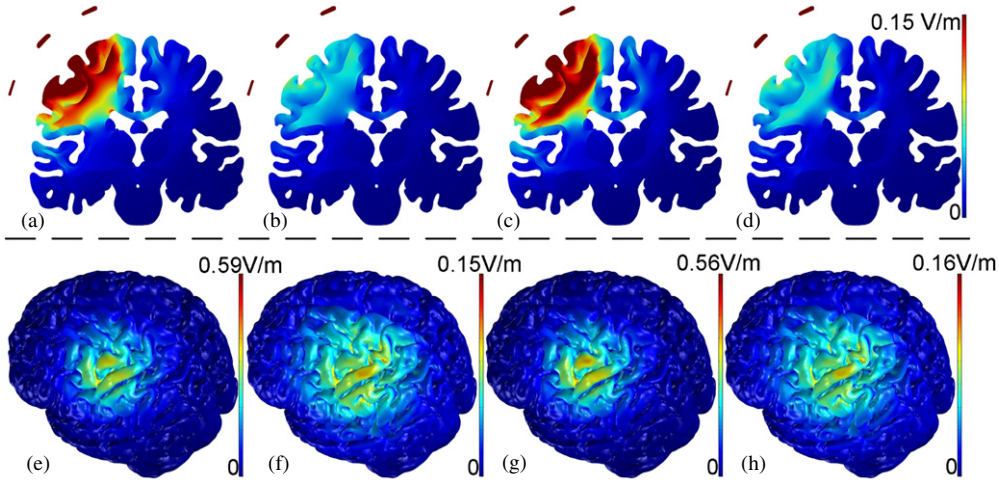

Figure 2. The effect of non-cortical and brain anisotropy on the strength and distribution of induced electric field under the high-definition montage m1. In (a)–(d), the posterior view of an arbitrary coronal slice has been selected and changes in *E*-field strength and distribution associated with various anisotropic regions under m1 configuration have been projected using a single scale. In (e)–(h), each model is represented by its individual E_{max} scale under m1 configuration. Slice (a) and 3D brain (e) illustrate *E*-field distribution under m1 montage using isotropic conductivities. (b) and (f) illustrate field distribution under the influence of skull and muscles anisotropic conductivities. (c) and (g) depict distribution under brain anisotropy. (d) and (h) show the combined influence of skull, muscles and brain anisotropy.

Table 2. The strength of electric field (median values) in various regions of the human brain under high-definition montage m1.

m1: 4 × 1 HD-montage with anode at C3				
Regions	Isotropic model E_{mediam} (mV m^{-1})	Model with skull and muscle anisotropy E_{mediam} (mV m^{-1})	Model with brain anisotropy E_{mediam} (mV m^{-1})	Model with skull, muscles and brain anisotropy E_{mediam} (mV m^{-1})
GM	8.0	7.0	7.8	7.0
WM	12.7	10.4	13.0	10.8
Hind brain	3.3	3.9	3.3	3.9
Fornix crura	11.7	8.8	12.0	9.0
Hippocampus	4.6	4.3	4.5	4.3
Thalamus	9.0	6.5	9.1	6.6
Putamen	7.9	6.5	8.5	7.1
Caudate nucleus	8.4	6.4	8.5	6.5

3. Results

3.1. Effects of anisotropic conductivity on induced electric field

Initially the high-definition montage m1 (4 × 1 HD-montage with anode at C3) was used to analyse the specific effects of non-cortical (skull and muscle of mastication) and brain anisotropic conductivity on the brain electric fields. Compared to the isotropic case, the inclusion of the skull and muscle anisotropy reduced the average electric field strength in the GM by 13% and in the WM by 20% (table 2). Compared to the isotropic case, inclusion of only the brain anisotropy in the model reduced the average GM electric field strength by 2.5% and increased the WM electric field strength by 2.3%. Inclusion of both the non-cortical and brain anisotropy reduced the average GM electric field strength by 13% and 16.2% in the WM, when compared to the isotropic model.

Qualitative changes in the electric field intensity and distribution following the inclusion of anisotropy are illustrated in figure 2. Compared to the isotropic case (figures 2(a) and (e)), consideration of only skull/muscle anisotropy resulted in a global absolute decrease in electric field strength (figure 2(b)) and an increase in relative spread along the cortex (figure 2(f))—both presumably reflecting increasing current shunting at supra-cranial levels. Compared to the isotropic model, the most evident change following the consideration of only the brain anisotropy was the enhanced electric field along WM tracts, notably the left pyramidal tract (figure 2(c)). The grey matter did not show any qualitatively notable degree of field variation (figure 2(g)). Inclusion of skull, muscle and brain anisotropy resulted in qualitative changes consistent with the collective actions (figures 2(d) and (h)). These results corroborate and expand upon previous modelling studies on the role of anisotropy (Oostendorp *et al* 2008, Shahid *et al* 2012, Suh *et al* 2012).

We next analysed the influence of anisotropy (non-cortical and brain) in the three considered montages. Under both isotropic and anisotropic (non-cortical and brain) conditions, in 4 × 1-ring montage m1, high *E*-field regions were confined in the proximity of the anode (C3) circumscribed by the outer-electrode ring (figures 3(d) and (g)), whereas, in 4 × 1-ring montage m2, high field regions were observed around the precentral and the superior frontal gyri, in the proximity of the anode C1 and within the ring (figures 3(e) and (h)). In montage

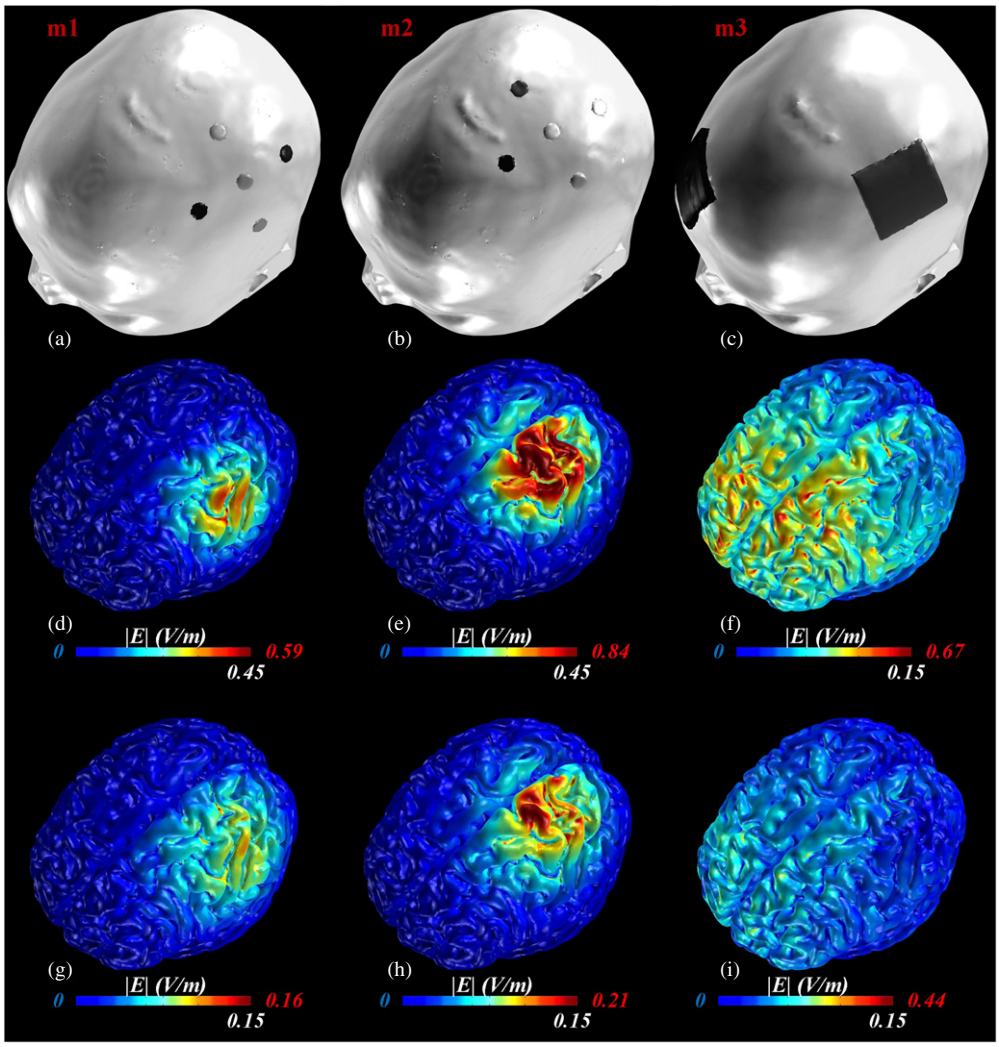

Figure 3. Role of electrode montage on the site and strength of induced electric field. (a) High-definition 4 × 1 montage m1 with anode located at C3. (b) High-definition 4 × 1 montage m2 with anode located at C1. (c) Conventional bi-cephalic montage m3 based on 5 × 5 cm^2 electrode pads. In m3, anode is positioned at C3 and the cathode is placed at the approximate location of Fp2. (d)–(f) Depiction of cortical electric field strength and distribution patterns of isotropic models under considered montages. (g)–(i) Depiction of the cortical electric field strength and distribution patterns of anisotropic models (skull, muscles and brain) under considered montages. (For each volume plot, the colour scale has two maximum values. The one at the top indicates the maximum value of the electric field and the bottom one indicates the value at which the plot was rescaled for better visualization.)

m2, the location of the anode and its proximity to the superior sagittal sinus, which was assigned the conductivity of the CSF, channelled more current through the inter-hemispheric fissure generating additional clusters of high *E*-field in the corpus callosum (figures 4(b) and (e)). Under both isotropic and anisotropic conditions, the current flow generated by the conventional tDCS montage m3 was mostly distributed around and between the electrodes (figures 3(f) and (i)).

The magnitude (residual error) and topographic (relative difference measure) variations in induced electric fields due to the inclusion of non-cortical and brain anisotropy under the three considered montages were also quantified in tables 3–5. For montages m1 and m2, the highest magnitude and topographic variations due to the combined effect of (cortical and non-cortical) anisotropy were observed in the GM followed by the WM. In sub-cortical regions, magnitude variations in the range of 10–40% and topographic errors in the range of 5–20% were observed. In the case of montage m3, the highest variations (residual error = 55; relative difference measure = 16%) were observed in the WM region.

The impact of tissue anisotropy on the input impedance (stimulator output) was also examined. In the high-definition montages (m1 and m2), the effect of skull and muscle anisotropy resulted in 1.5% increase in the input impedance. On the other hand, in conventional montage m3, the skull and muscle anisotropy increased the input impedance by 21%. In the three considered montages, the influence of brain anisotropy on the input impedance was calculated to be less than 0.1%. Using the integral of *J* across the cathodes surfaces of both high-definition montages, the return currents to individual cathodes were determined. Table 6 shows the proportion of the return current to the individual cathodes in high-definition montages. It is worth mentioning that, under high-definition montages, the effect of anisotropy (skull,

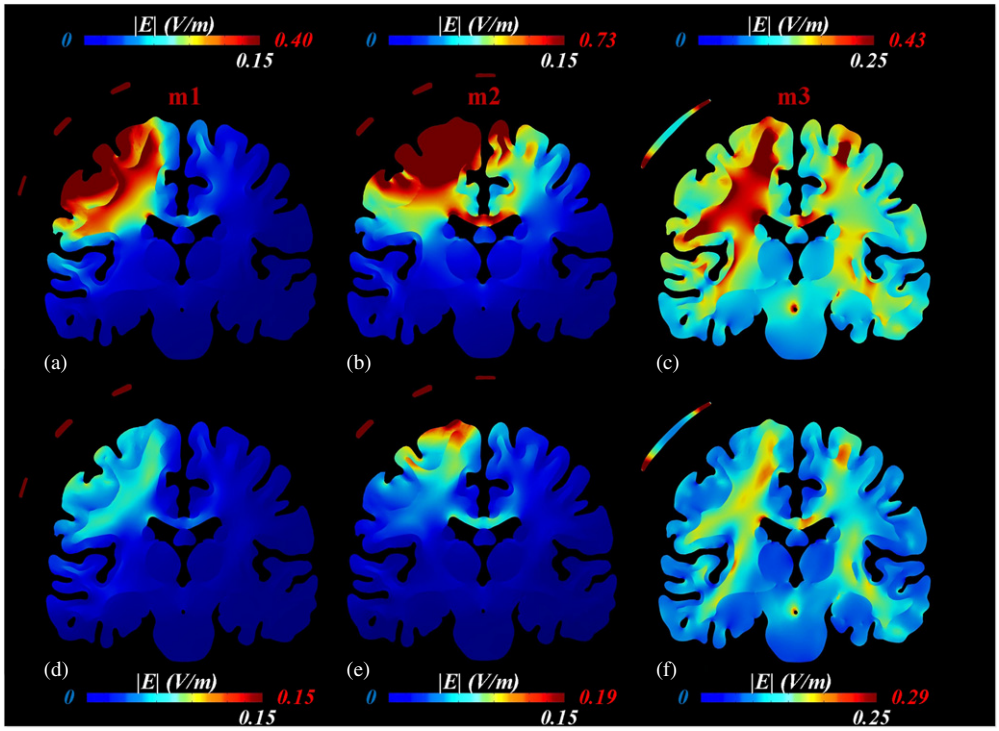

Figure 4. Posterior view of an arbitrary coronal slice depicting (a), (b) and (c) electric field strength and distribution patterns of isotropic models under considered montages. (d)–(f) Illustration of electric field intensity and distribution patterns of anisotropic (skull, muscle and brain) models under considered montages. (For each slice plot, the colour scale has two maximum values. The one at the top indicates the maximum value of the electric field and the bottom one indicates the value at which the plot was rescaled for better visualization.)

Table 3. Magnitude (RE) and topographic (RDM) errors in the induced electric field of the volume conductor model due to the inclusion of skull, eye muscles, muscle of mastication and brain directional electric conductivity. The electrode configuration is 4 × 1 high-definition with anode at C3 and four cathodes around C1, C5, FC3 and CP3.

m1: 4 × 1 HD-montage with anode at C3						
	Iso versus skull and muscle anisotropy		Iso versus brain anisotropy		Iso versus skull, muscles and brain anisotropy	
Regions	RE	RDM	RE	RDM	RE	RDM
GM	147.2	34.5	5.0	4.9	146.1	36.1
WM	121.3	31.1	9.9	8.7	111.5	34.1
Hind brain	23.3	23.4	6.7	6.3	23.3	23.5
Fornix crura	44.3	9.9	4.3	4.1	42.7	11.1
Hippocampus	20.0	11.7	4.3	4.1	21.6	13.1
Thalamus	42.9	7.1	4.1	4.1	45.3	8.1
Putamen	34.6	10.9	7.7	6.7	29.2	14.0
Caudate nucleus	43.9	16.1	9.3	7.9	37.7	15.7

Table 4. Magnitude (RE) and topographic (RDM) errors in the induced electric field of the volume conductor model due to the inclusion of skull, eye muscles, muscle of mastication and brain directional electric conductivity. The electrode configuration is 4 × 1 high-definition with anode at C1 and four cathodes around Cz, C3, FC1 and CP1.

m2: 4 × 1 HD-montage with anode at C1						
	Iso versus skull and muscle anisotropy		Iso versus brain anisotropy		Iso versus skull, muscles and brain anisotropy	
Regions	RE	RDM	RE	RDM	RE	RDM
GM	100.9	24.8	4.6	4.6	101.3	26.3
WM	94.9	22.6	8.0	7.3	88.9	25.3
Hind brain	21.5	21.5	6.1	5.1	23.0	21.9
Fornix crura	24.5	8.3	5.9	5.5	21.1	9.8
Hippocampus	13.3	11.9	3.9	3.9	13.7	13.4
Thalamus	28.1	5.1	4.6	3.9	30.2	7.1
Putamen	28.6	15.2	10.1	8.9	30.2	21.3
Caudate nucleus	28.7	12.9	6.4	6.1	27.0	16.6

Table 5. Magnitude (RE) and topographic (RDM) errors in the induced electric field of the volume conductor model due to the inclusion of skull, eye muscles, muscle of mastication and brain directional electric conductivity. The electrode configuration is conventional C3-Fp2.

m3: C3-Fp2 conventional electrode montage						
	Iso versus skull and muscle anisotropy		Iso versus brain anisotropy		Iso versus skull, muscles and brain anisotropy	
Regions	RE	RDM	RE	RDM	RE	RDM
GM	63.5	15.6	6.5	6.4	62.6	16.7
WM	64.7	13.3	12.2	10.2	55.1	16.3
Hind brain	24.9	11.6	5.4	5.2	23.5	12.3
Fornix crura	49.9	6.9	4.5	4.4	49.3	9.4
Hippocampus	39.7	4.3	6.3	5.6	43.2	6.9
Thalamus	45.3	3.1	6.6	6.2	49.5	7.3
Putamen	52.1	3.4	10.7	9.8	46.5	8.3
Caudate nucleus	51.9	7.8	7.9	6.9	46.9	9.7

Table 6. Return current distribution among cathodes in HD-montages.

Electrode location	Montage m1 (skull, muscle and brain anisotropic)	Electrode location	Montage m2 (skull, muscle and brain anisotropic)
C1	21.3%	Cz	29.1%
C5	26.7%	C3	18.2%
FC3	30.0%	FC1	26.2%
CP3	21.0%	CP1	26.5%

muscle and brain) on return current distribution was less than 0.1% (due to the close proximity of electrodes).

3.2. Clinical relevance of model complexities

Under the isotropic conditions, replacing the montage m1 by m2 resulted in a reduction of 7.7% in the averaged electric field strength across the M1 region. For the brain anisotropic model, montage replacement resulted in a drop of 8.4% and for model with non-cortical anisotropy, the replacement of montage increased the average electric field value by 9.6% across the motor cortex region. The inter-montage comparison between the isotropic models of m1 and m3 showed the drop of 56.4% in the average electric field across the M1 region. For brain anisotropic models, the inter-montage variation (m1 versus m3) resulted in a drop of 56.1% in the electric field strength across the M1 area and models with skull and muscle anisotropy resulted in a drop of 75.8% across the M1 region. Therefore, the maximum inter-montage difference, in the electric field strength across the M1 region, due to the inclusion of anisotropy was 20% (m1 versus m3). Similarly, by comparing the other two regions of interest, the maximum inter-montage variation due to anisotropy was not more than 20% (table 7). These anisotropy related variations should change the estimated local current flow pattern in the ROIs (inter-montage analysis of the influence of anisotropy); however, our analysis suggests that inter-montage variations (for clinicians considering which montage to select) were not significantly influenced by the inclusion/exclusion of anisotropy. Thus, for the considered HD-montages, quantitative changes in the electric field due to the inclusion of anisotropy do not necessarily equate to meaningful changes as far as clinical dose decisions across HD-montages are concerned (montage selection).

3.3. Assessment of the electric field along fibre tracts

Under the assumption that neuromodulation in a particular brain region or a network of neurons can be predicted by a function of the induced electric field, we considered three possible representations of neuromodulation based on the induced electric field. The consideration of only electric field/current density is common in the tDCS modelling literature following the quasi-uniform assumption (Bikson *et al* 2012a), but more precise functions of the electric field have been proposed when morphological and/or diffusivity data are available (Chaturvedi *et al* 2010, 2012, Lujan *et al* 2008, 2012, Silva *et al* 2008). In this study, we assumed that diffusion-weighted MRI (DWI) could be used to estimate the fibre structures of major WM tracts. These connectivity estimations based on the deterministic scheme (Jiang *et al* 2006) were used to examine the influence of the three considered activating functions (λE_P, $\lambda^2 \partial E_P/\partial l$—equation (10) and $\lambda(\Delta E_P/2)\, e^{-|l|/\lambda}$—equation (11)) on membrane (de-/hyper-) polarization. The fibres were defined along the superior (start of tract)–inferior (end of tract) frame of reference. By comparing activating functions across exemplary montages along selected fibre tracts, we intended to access (in principle) whether representations of neuro-polarization (instead of simply electric field) provide further insight into montage selection (figure 5, supplementary figure 1 (available from stacks.iop.org/JNE/11/036002)) and whether the inclusion of additional modelling complexity based on neuronal morphology increases the clinical utility of computational models.

In this study (inter-montage) variations in the activating function (λE_P) and its associated functions (equations (10) and (11)) were assessed based on the orientation of the induced electric field (derived from full anisotropic models) relative to the fibre architecture and conductivity variations. In the considered HD-montages (figure 5), the left corticospinal tract exhibited the maximum membrane polarization (λE_P), ranging from 40 μV (m1) to 67 μV (m2) (figure 5, columns 2 and 6). For the conventional montage m3, the left corticospinal tract exhibited the maximum polarization (hyper/de) of 115 μV

Table 7. Ranking based on the selected regions of interest.

Montage	Isotropic model	Model with only skull and muscle anisotropy	Model with only brain anisotropy	Model with both non-cortical and brain anisotropy
		E_{median} (mV m^{-1})		
		ROI-M1		
m1	76.1	33.5	75.4	33.1
m2	70.4	36.9	69.3	36.8
m3	135.9	74.4	134.2	73.4
		ROI-Contralateral M1		
m1	9.1	7.5	8.7	7.4
m2	18.4	13.6	17.9	13.5
m3	110.6	71.3	112.4	72.4
		ROI-SMA		
m1	29.0	16.0	29.6	16.4
m2	41.2	23.4	41.4	23.5
m3	202.0	104.6	210.1	108.7

and over all genu of corpus callosum displayed the maximum membrane polarization (λE_P) of 565 μV (supplementary figure 1 (available from stacks.iop.org/JNE/11/036002), column 2). For the HD-montage m1, the strongest de-/hyper-polarization associated with an abrupt change in $\boldsymbol{E_P}$ ($\lambda^2 \partial E_P/\partial l$) and discontinuity in tissue conductivity ($\lambda(\Delta E_P/2)\,e^{-|l|/\lambda}$) was traced along the stretches of the left corticospinal tracts and the medial of corpus callosum, respectively (figure 5, columns 3 and 4). For the HD-montage m2, the right corticospinal tracts showed the highest strength of membrane polarization due to an abrupt change in $\boldsymbol{E_P}$ ($\lambda^2 \partial E_P/\partial l$) and medial of corpus callosum was associated with maximum de-/hyper-polarization due to conductivity variations (figure 5, columns 7 and 8). For the bi-cephalic montage m3, genu of corpus callosum displayed the maximum field variation associated with a strong jump in $\boldsymbol{E_P}$ and discontinuity in tissue conductivity.

Using single fibre analysis, the influence of electrode montage (electric field orientation) and tissue conductivity variation was further explored. The selected fibre was from the L-CST. The magnitude of the induced electric field, activating function (λE_P), derivative of the activating function ($\lambda^2 \partial E_P/\partial l$), modulation function associated with conductivity profile ($\lambda(\Delta E_P/2)\,e^{-|l|/\lambda}$), fractional anisotropy (*FA*) and electrical conductivity profile were traced along the path of the selected fibre (figure 6). Comparing the $\boldsymbol{E_P}$ profile along the selected fibre, under the selected montages, it was observed that the strength and possible locations of de-/hyper-polarization (λE_P and $\lambda^2 \partial E_P/\partial l$) were highly sensitive to the orientation of the induced electric field ($\boldsymbol{E}$) with respect to the fibre path. Similarly, variations in *FA* and conductivity plots highlighted the influence of tissue conductivity in shaping the neuromodulation ($\lambda(\Delta E_P/2)\,e^{-|l|/\lambda}$).

Finally, to analyse the contribution of axonal/fibre bend in regulating de-/hyper-polarization, artificial bends were introduced (at the boundary of GM-WM) on selected fibres of the L-CST (figure 7). It was assumed that these fibres tend to project normal to the local WM boundary. In the presence of a uniform (at mesoscopic scale) electric field ($\boldsymbol{E}$), an abrupt change in fibre path caused variations in the strength of $\boldsymbol{E_P}$. For HD-montages m1 and m2, variations in $\boldsymbol{E_P}$ and its gradient ($\lambda^2 \partial E_P/\partial l$) due to the artificially induced bends were predicted (figure 7). Since each fibre tract displayed a unique orientation with respect to the induced electric field ($\boldsymbol{E}$), each fibre exhibited a distinctive strength and direction of the gradient of $|\boldsymbol{E_P}|$. This observation concurs with the findings of Kabakov *et al* (2012). For example, the same fibres in montages m1 and m2 displayed different responses (λE_P and $\lambda(\Delta E_P/2)\,e^{-|l|/\lambda}$) owing to the unique distribution patterns of the induced electric field. For the selected HD-tDCS montages, percentage differences in E_P along five selected fibres at three equally spaced points were calculated (table 8). Compared to the E_P of fibre 1 (f1), under both HD-montages, the percentage differences were recorded in the range 0.3–50%. These variations in activating functions signify the role of neuronal morphology in deciphering the locus of modulation. As observed from the considered montages, the maximum of field strength and associated activating functions were not always located directly underneath the anodes and such a prediction is not possible by just relying on scalar field maps. Neuro-navigation scheme based on fibre tractography would be highly significant to optimize tDCS dose parameters, especially in modulating deep brain regions associated with migraine and tinnitus pathophysiology (Dasilva *et al* 2012, Parazzini *et al* 2012a).

Table 8. Percentage differences in E_P along the selected fibres.

	Montage m1		
	Calculation points along the fibre pathways		
Comparison (percentage difference)	5 mm	10 mm	15 mm
f2–f1	48.1	9.9	1.5
f3–f1	27.2	7.7	14.9
f4–f1	29.9	3.1	17.5
f5–f1	51.4	0.5	9.4
Montage m2			
f2–f1	3.0	5.2	3.1
f3–f1	14.2	9.9	3.4
f4–f1	25.8	20.3	11.1
f5–f1	5.6	0.3	1.3

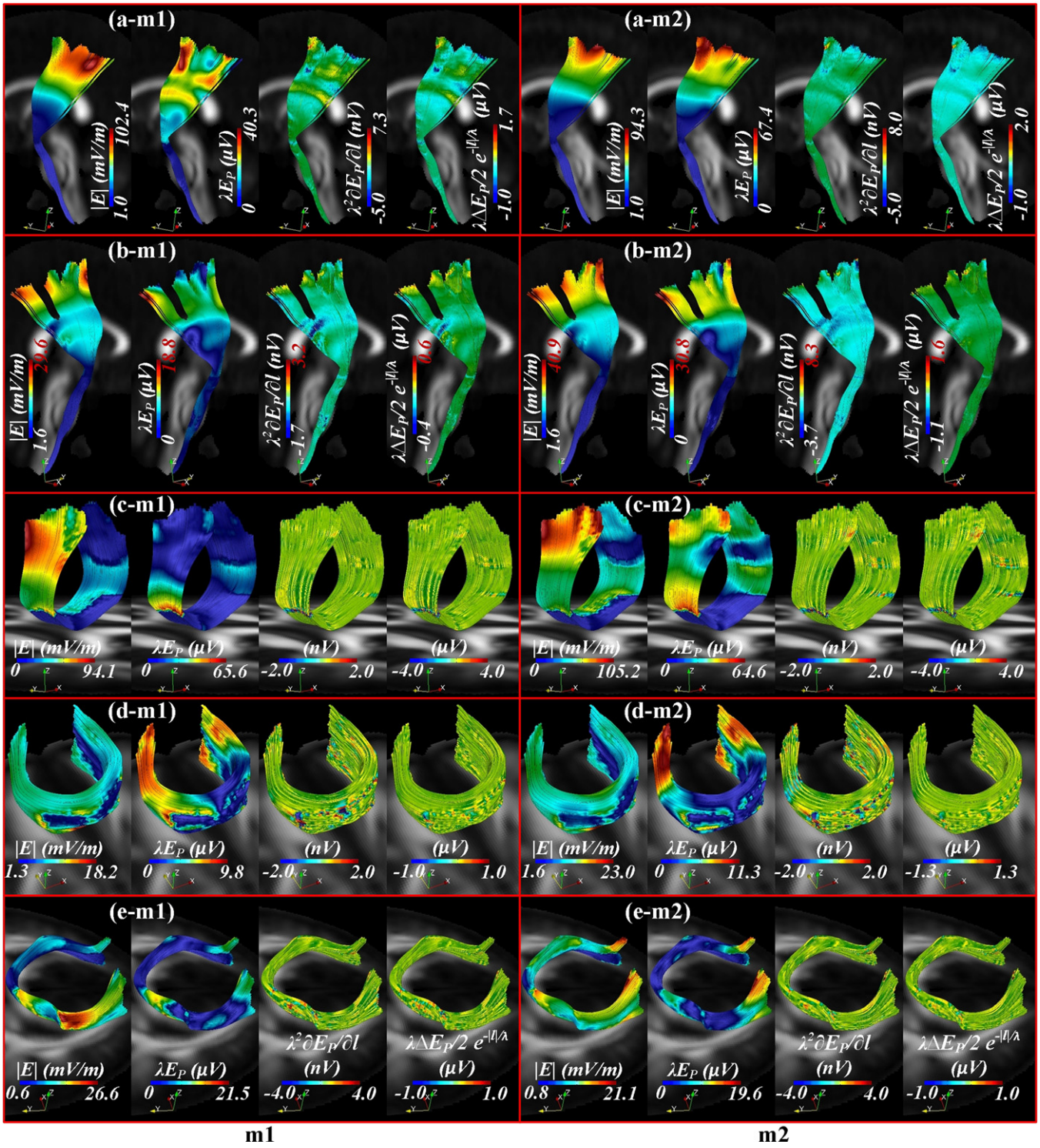

Figure 5. Montage specific behaviour of induced electric field E and stimulation parameters λE_P, $\lambda^2 \partial E_P/\partial l$ and $\lambda(\Delta E_P/2)\mathrm{e}^{-|l|/\lambda}$ across (a) left corticospinal tracts, (b) right corticospinal tracts, (c) medial of corpus callosum, (d) genu of corpus callosum and (e) splenium of corpus callosum under HD montages m1 and m2, respectively ($\lambda = 1$ mm). The induced electric field was obtained from the anisotropic (non-cortical and brain) models.

4. Discussion

The objective of this study was to consider when additional imaging and modelling complexity (cost) results in predictions that have distinguishing clinical values. As such, we note that the montages selected were exemplary and the metrics for analysis and scoring are not proposed as definitive—indeed variations in modelling methods further emphasize the need for vigilance in valuing complexity. Our discussion of the broader relevance of this work thus includes (1) general points on modelling details and approaches, illustrating DTI/fibre tractography, (2) consideration of the cost (time and resources) of complexity and, (3) balance against a paradigm we proposed for evaluating additive clinical value of complexity.

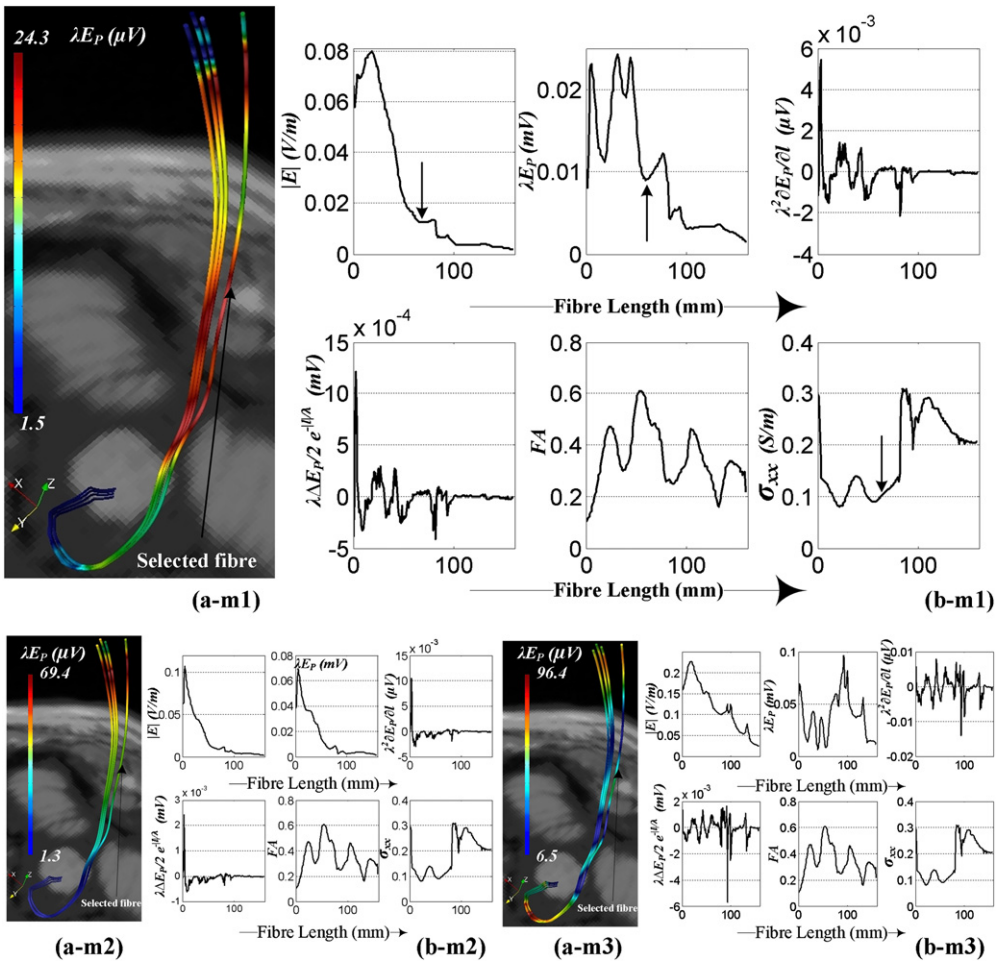

Figure 6. Single fibre level investigation using the projection of induced electric field 'E', stimulation parameters λE_P, $\lambda^2 \partial E_P/\partial l$ and $\lambda(\Delta E_P/2)\,e^{-|l|/\lambda}$, fractional anisotropy index 'FA' and conductivity distribution along the selected fibre (a-m1 and b-m1) under HD-montage m1, (a-m2 and b-m2) for HD-montage m2 and (a-m3 and b-m3) for bi-cephalic montage m3. In each section (m1, m2 and m3), sub-part (a) illustrates E_P along the selected fibres of left cortico-spinal tract and (b) highlights the variations in field parameters, FA and anisotropic conductivity along the selected fibre ($\lambda = 1$ mm).

4.1. Improvement in predictive modelling by incorporating tissue anisotropy and fibre tractography

The results of this study emphasize that the sites and strength of the induced E-field are highly sensitive to the variations in the distance between the electrodes, the electrode sizes and arrangements (configurations), and the relative position of electrodes (both anode and cathodes) with respect to the ROI (Bikson *et al* 2010, Datta *et al* 2011, Shahid *et al* 2014). Brain anisotropic conductivity could facilitate regional field enhancement or attenuation and the intensity of such a variation depends upon the degree of alignment between the induced current and the local conductivity profile. In general, skull anisotropy causes a shunting effect, leading to a reduction in the strength of the induced E/J in the brain and sub-cortical regions (Bai *et al* 2012, Shahid *et al* 2012, Suh *et al* 2012). In HD-tDCS montages, high electric field regions were restricted by the outer electrode rings. The close proximity of return electrodes, the shunting effect of skull directional conductivity and local variations in the thickness of superficial layers, all corroborated high values of RE and RDM, when compared to the conventional montage (tables 3–5). It is imperative to understand that the neural response to the induced E-field is not only dependent on the strength of the induced field, but also on the electrophysiological parameters, morphology and orientation of neurons relative to the induced electric field. To estimate the impact of neural orientation on the site and strength of modulation, the DTI information used in the conductivity estimation was employed to perform fibre tracking on the selected ROIs. Such information is vital to understand the orientation specificity of different electrode montages.

In this study, we have tried to address the importance of anisotropic electric conductivity associated with various regions of the head model using clinically available modalities. The emphasis has also been laid on the best practice to use these modalities to translate the strength and spatial distribution of the electric field from spatial plots to three-dimensional fibre tracts. This translation is quite significant to address the issue of current polarity and neuromodulation along the major fibre tracts of the white matter. Thus, in translating prediction of current flow to polarization (as a first step towards predicting neuromodulation), the role of realistic conductivity distribution should not be overlooked. Additionally, inclusion

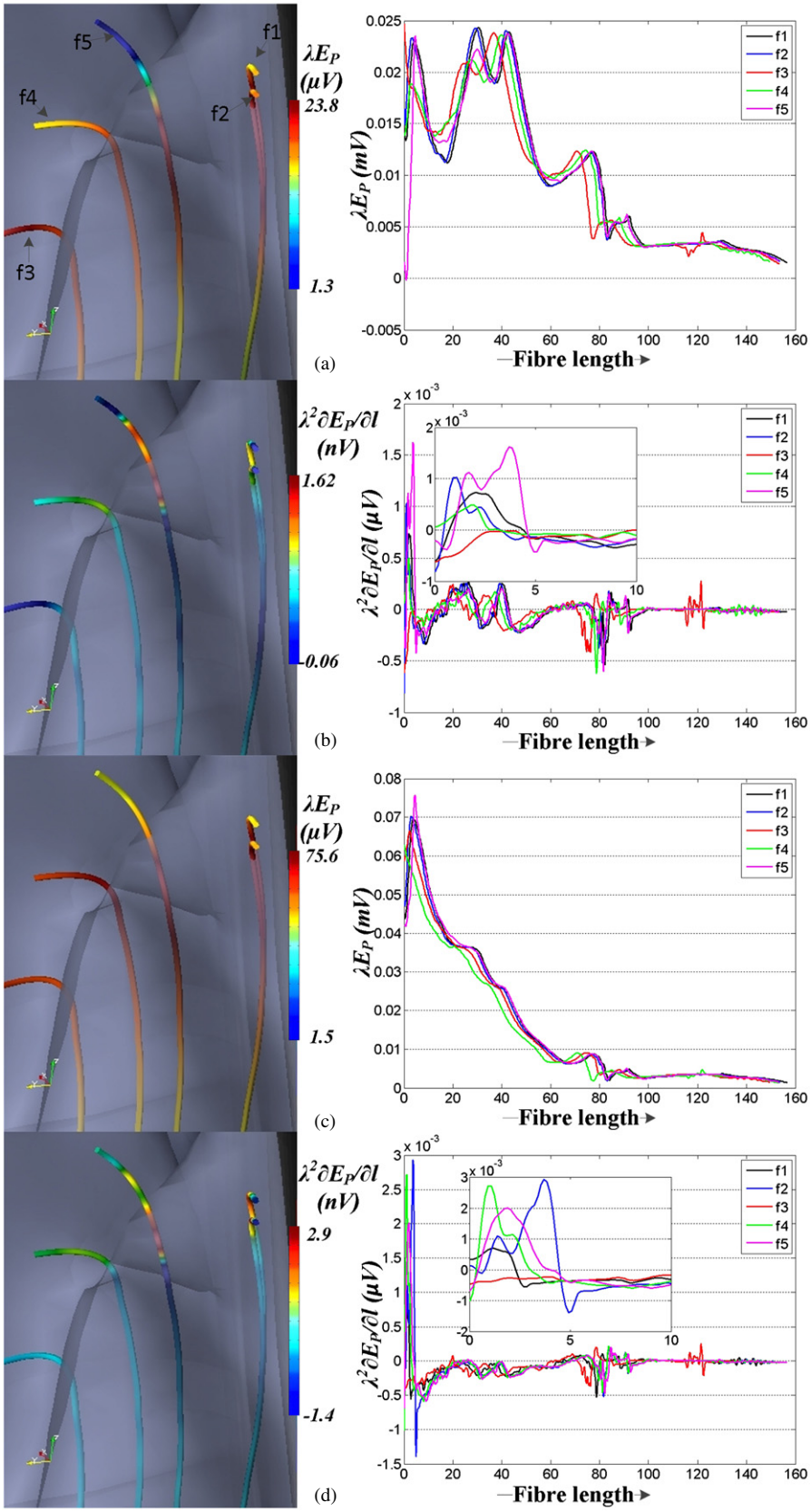

Figure 7. Behaviour of stimulation parameters λE_P and $\lambda^2 \partial E_P / \partial l$ in the presence of artificial bends ($\lambda = 1$ mm). (a) and (b) montage m1, (c) and (d) montage m2.

of brain anisotropy and fibre tractography can further extend our understanding of stimulus influence from particular ROI to brain functional connectivity and neural connections (Antal *et al* 2011, Polania *et al* 2012, Zheng *et al* 2011).

4.2. Clinical costs/benefits for incremental model complexity: evaluating cost

With endless room for increased modelling complexity and precision, the pivotal question, which has rarely been addressed, is the potential clinical utility of incorporating such model complexities versus the cost involved. When do the clinical benefits of including such intricate details justify the issues such as computational costs, scan time and pre-/post-processing time etc. First, we need to consider the technical and clinical cost in predicting current flow, then the value in context of current clinical practise and thirdly, the incorporation of multi-scale analysis.

Regardless of approach and complexities, all forward models estimate current flow during stimulation. First, even before considering the value of complexity, the field variations associated with segmentation errors and conductivity assignment must be considered. These errors, if not properly mitigated, could be much higher than those associated with anisotropy. Errors related to tissue misclassification or conductivity assignment are important; however, they should not impede the improvements in other fields of predictive modelling. Importantly, our consideration of cost is based on incremental effort over baseline tissue classification. Secondly, additional complexity does not guarantee increased accuracy, for example, we recently showed significant differences in the methods of modelling WM anisotropy (Shahid *et al* 2013). We assume that the rational inclusion of anisotropy will tend to increase the model accuracy to some degree.

An important step in the incorporation of brain anisotropy in head models requires the acquisition and post-processing of DTI sequences. On modern scanners, for instance, a Jones20 DTI sequence with 1.85 mm isotropic DTI resolution takes about 8 min (extra acquisition time) (Jones *et al* 1999). Similarly, the post-processing of DWI, which involves steps such as artefact removal (due to eddy currents and subject motion), reorientation of gradient directions after the affine registration (required after performing the artefact removal) (Leemans and Jones 2009), EPI artefact removal (susceptibility artefacts) (Ruthotto *et al* 2012), calculation of diffusion parameters (eigenvalues, eigenvectors and fractional anisotropy indices), co-registration of tensor maps to high-resolution scalar volumes and orientation correction due to co-registration, altogether require no more than 3–5 min (Ruthotto *et al* 2012). The translation of the diffusion tensor to conductivity tensor can take an additional 1–2 min. The main bottleneck in current forward modelling schemes is the segmentation of scalar volumes, which can take from a few minutes (automated but unreliable) to a few days (manual or semi-automated segmentation). So adding complexity in terms of diffusion tensors does not add much relative time in pre-processing; on the other hand, it does add value by redefining the local current paths in the volume conductor model. More advanced conductivity-based refinements such as incorporation of HARDI or DSI schemes in volume conductor models are, at the moment, practically not feasible in clinical environment. Based on the study of Hagmann *et al* (2006), the acquisition time of 30 axial slices of 3 mm thickness would be between 10 and 20 min for HARDI ($b > 1000$ and number of measurements >60) and 15 and 60 min for DSI ($b > 8000$ and number of measurements >200). However, 3 mm thickness is too coarse to extract any meaningful information. Usually, in practice 2 mm slice thickness is preferred; however, such complex acquisitions will end up in substantially larger datasets and acquisition time in hours, which is clinically not feasible. Thus, the cost of complexity may largely be a clinical study burden, especially if individualized scans are desired.

Another argument against the increase in model complexity (increased mesh density and anisotropy) is the increase in computation load (Kybic *et al* 2005, Plis *et al* 2007, Fuchs *et al* 2007). The computational cost is highly solver dependent. Wolters (2003) demonstrated that for a fixed accuracy rate, the computation time for CG pre-conditioned by Jacobi increased from 650 iterations (isotropic) to 850 iterations (anisotropic), whereas, CG pre-conditioned by AMG maintained 15 iterations in both isotropic and anisotropic solutions. Hence, with appropriate pre-conditions the computational load margin between isotropic and anisotropic simulations can be reduced significantly (Rullmann *et al* 2009). Evidently, the actual computational cost depends on available technology and resources, and it seems reasonable to speculate these will become less burdensome in the next few years, even without innovation in specialized algorithms (Dmochowski *et al* 2011).

An increasingly complex modelling approach may be considered to have incremental clinical value if it either prospectively informs clinical dose or retrospectively informs study interpretation (which brain regions were targeted). While evidently changing the model will change the resulting predictions, if these changes do not influence clinical practise then their value is purely academic. It is therefore incumbent to consider exactly how modelling may influence clinical practise.

A priori, we assume that added detail/complexity will enhance model precision and, if done rationally, model accuracy (Bikson *et al* 2012b, 2012c). Although an engineering group can devote extended resources and time to a 'case' modelling study, the myriad of potential electrode combinations (dose) and variation across a normal head (Datta *et al* 2012) and pathological heads means that in clinical trial design the particular models will likely now be solved. Moreover, while 'different models will yield different predictions' practical dose decision is based on a clinical study specific criterion: 'a meaningful clinical difference'. We thus consider two clinical applications of modelling. (1) Deciding across montages—namely which montage is expected to achieve the optimal clinical outcomes in a given subject or on average across subjects; (2) deciding on dose variation across subjects—namely if and how to vary dose based on the

subject specific anatomy. We focus here on the first clinical application and on the question of if added complexity in the model, associated with increased computational cost per simulation, is clinically warranted. The second application, we did not address specifically here because current clinical practice does not individualize dose, limited in part by the cost associated with collecting and processing even the most basic individual models (e.g. without anisotropy). However, the methods we develop are equally applicable to this second application. It is further necessary to consider if the clinician is concerned with optimizing (a) intensity at the target (maximum current at the target regardless of overall brain current flow) or/and (b) focality at the target (intensity at the target relative to other brain regions). Consideration of intensity or focality may lead to fundamentally different 'best' dose (Dmochowski *et al* 2011). In the first application, the clinician will compare different montages for their intensity and/or targeting of a brain region. Therefore, additional complexity and detail is only clinical meaningful if it results in a different selection of optimal montage based on either intensity or focality criterion.

Finally for targeting, based on current practices, a clinician is typically not concerned with minutia of current flow patterns, but on a general ranking of which regions are more or less activated. In this paper, clinical regional ranking has thus contrasted with statistical indices. Our overall preposition, developed in this paper is thus: because in clinical trial design modelling complexity costs time and resource, it is justified only when the selection of the optimal montage based on either intensity and/or targeting (regional ranking) changes.

4.3. Limitations

Validation of forward solutions for EEG, TES and TMS against clinical data remains a challenge. Recently, some efforts have been made for the validation of EEG forward modelling (Bangera *et al* 2010), TES (Datta *et al* 2013, Edwards *et al* 2013) and TMS (Opitz *et al* 2013). These direct physiological validation schemes support the forward modelling paradigms. Since these volume conductor models obey Maxwell's equations (laws of physics), the main aspects of their assessments do not change, even though (within the bounds of the defined boundary conditions) these models may provide different outcomes.

In predictive modelling, anatomical features and tissue dielectric properties play a crucial role in defining the resulting electric field. Most often model-based brain stimulation studies rely on a single subject dataset, as under similar stimulation parameters, the inter-subject trends in magnitude and topographic variations exhibit similar behaviour (Parazzini *et al* 2012b, Shahid *et al* 2013). Thus, it is possible to postulate on the validity of single subject results across multiple subjects.

In TES, the relatively low conductivity of skull plays a crucial role in defining the magnitude and distribution of field parameters. Human skull is composed of three distinguishable regions, spongoasa, enclosed in compacta bone and the idea of skull anisotropic electrical conductivity behaviour is associated with its layered composition. Since it is not easy to classify the diploe region of skull by using MRI data alone, therefore, most of the studies in forward head modelling consider skull as a homogeneous anisotropic region (Wolters *et al* 2006, Suh *et al* 2012) or homogeneous isotropic domain (Datta *et al* 2009, Shahid *et al* 2013). According to the experiment conducted by Rush and Driscoll (1968), the ratio of saline conductivity to skull conductivity in the radial direction varied from 1:50 to 1:300 and 1:5 to 1:40 in the tangential direction. Studies by De Munck (1988), Marin *el al* (1998) and Munck and Peters (1993) reported anisotropic skull behaviour with a conductivity variation of 1:10 (i.e., the conductivity in tangential direction is ten times the conductivity in radial direction). A more recent study by Sadleir and Argibay (2007) reported the sub-optimal response of such schemes. In their opinion, a three-layer isotropic skull provided close agreement with the *in vivo* measurements of skull electrical conductivity. More recently, Dannhauer *et al* (2011) reported the significance of local variations in skull conductivity for EEG forward and inverse solutions. Under the hypothesis that optimal conductivity values are primarily dictated by the equivalent radial conductivity of the three-layered skull, Rampersad *et al* (2013) suggested the validity of both anisotropic and isotropic approximation when dealing with cortical electric field parameters. However, there is no experimental evidence to support this hypothesis.

Since the idea behind this study was to employ clinically available modalities, which are used frequently in physiological examination, therefore, incorporation of CT scans in head model construction was not considered. Without the use of CT scans, further improvements in skull segmentation can be achieved by, perhaps, employing ultra-short TE (UTE) MRI sequences in the head model construction (Wang *et al* 2010).

In this study, activating functions were derived from the induced electric field (E); therefore, the accuracy and quality of these results (along the stretches of fibres) are highly susceptible to numerical errors. The finite element method provides an approximate solution. In this study, the convergence criterion was defined by the global error tolerance of 10^{-8}. So even after the solution has converged, differences to the actual solution will always remain. In this study, we used linear basis functions. Higher order basis functions generally increase numerical accuracy; however, use of higher order basis functions and increase in mesh density has a significant effect on overall computational resources (Shahid and Wen 2010). Since there are no analytical solutions of TES available that deal with complex geometries, therefore, in this study, we evaluated the accuracy of the solutions by assessing the variations between the injected current and the return current.

In this study, the fibres were considered unmyelinated and their morphological response and neural activation dynamics in the presence of external stimulus were not considered. At present, there are no computational models that can realistically simulate the neural response to a weak electric current. However, using a simplified cortical model, Salvador *et al* (2011) reported the electrophysiological response of various cortical neurons in a uniform E-field. Therefore, the next logical step would be to incorporate the mathematical models of neural responses and membrane kinetics in FE models to identify possible sites of neural excitation.

In this study, the brain anisotropic conductivity estimation was carried out using the DTI data under the assumption that the diffusion tensor is second rank and symmetric. Such an assumption caused the regions of fibre crossing appear close to isotropic. The convoluted and inter-crossing branches of cortical neurons make it impossible to estimate actual fibre paths in low *FA* regions. To improve the conductivity estimation, it would be imperative to overcome the limitation of fibre crossing by using, perhaps, the orientation distribution function (ODF), which can be used to characterize the diffusion distribution (Yeh and Tseng 2011). Diffusion data may be acquired using high-resolution diffusion imaging scheme (Tuch *et al* 2002) or diffusion spectrum imaging (DSI) (Wedeen *et al* 2008). Alternatively, model-free reconstruction methods such as Q-ball (Tuch 2004) with DSI can be used to estimate the diffusion probability and diffusion ODFs. Since the fibre tracking performed in this study was based on the DTI data, therefore, it was only possible to track fibres in the regions of high *FA*. That is why the tracking was limited to the regions of $FA > 0.2$. However, by employing the probabilistic tracking rather than the deterministic scheme, it should be possible to deduce reliable information in low FA regions (Behrens *et al* 2003). Such a scheme can extend the scope of this study in low *FA* regions and would be able to provide the much-needed neural interaction information in the superficial regions of the brain.

Appendix A. Statistical indices used to estimate field variations under the considered montages

RDM is the measure of topographic variation (Meijs *et al* 2002). The minimum error corresponds to 0 and the maximum error corresponds to an RDM of 1. RDM is insensitive to the scaling variations among the datasets being compared, thus making it an ideal choice for comparison of distribution differences among field parameters:

$$\mathrm{RDM} = \sqrt{\sum_{i=1}^{n}\left(\frac{E_i^{\mathrm{BASELINE}}}{\sqrt{\sum_{i=1}^{n}\left(E_i^{\mathrm{BASELINE}}\right)^2}} - \frac{E_i^{\mathrm{VAR}}}{\sqrt{\sum_{i=1}^{n}\left(E_i^{\mathrm{VAR}}\right)^2}}\right)^2}. \tag{A.1}$$

Residual error (RE) (Gujarati 2003):

$$\mathrm{RE} = \sqrt{\frac{\sum_{i=1}^{n}\left(E_i^{\mathrm{BASELINE}} - E_i^{\mathrm{VAR}}\right)^2}{\sum_{i=1}^{n}\left(E_i^{\mathrm{VAR}}\right)^2}}, \tag{A.2}$$

where E_i^{BASELINE} is the baseline parameter (electric field of isotropic head models) and E_i^{VAR} represents the same field parameter (electric field of anisotropic head models) of different head models considered in the comparison. 'i' represents the total number of data points (elements of a particular subdomain or ROI).

Appendix B

Table B1. Voltages (in mV) applied/adjusted in different simulations to achieve the desired injected current (1 mA). In all cases, the initial voltage applied was 1 V.

Models	m1	m2	m3
Isotropic model	639.74	586.44	182.07
Model with skull and muscle of mastication anisotropy	651.51	595.73	233.11
Models with brain anisotropy	639.73	586.44	182.32
Models with both non-cortical and brain anisotropy	651.52	595.73	233.19

References

Akhtari M *et al* 2002 Conductivities of three-layer live human skull *Brain Topogr.* **14** 151–67

Antal A, Bikson M, Datta A, Lafon B, Dechent P, Parra L C and Paulus W 2012 Imaging artifacts induced by electrical stimulation during conventional fMRI of the brain *NeuroImage* **85** 1040–7

Antal A, Polania R, Schmidt-Samoa C, Dechent P and Paulus W 2011 Transcranial direct current stimulation over the primary motor cortex during fMRI *NeuroImage* **55** 590–6

Bai S, Loo C, Al Abed A and Dokos S 2012 A computational model of direct brain excitation induced by electroconvulsive therapy: comparison among three conventional electrode placements *Brain Stimul.* **5** 408–21

Bangera N, Schomer D, Dehghani N, Ulbert I, Cash S, Papavasiliou S, Eisenberg S, Dale A and Halgren E 2010 Experimental validation of the influence of white matter anisotropy on the intracranial EEG forward solution *J. Comput. Neurosci.* **29** 371–87

Basser P J and Roth B J 1990 Electromagnetic stimulation of a myelinated axon *Proc. 16th Annu. Northeast Bioengineering Conf.* pp 129–30

Basser P J and Roth B J 1991 Stimulation of a myelinated nerve axon by electromagnetic induction *Med. Biol. Eng. Comput.* **29** 261–8

Baumann S B, Wozny D R, Kelly S K and Meno F M 1997 The electrical conductivity of human cerebrospinal fluid at body temperature *IEEE Trans. Biomed. Eng.* **44** 220–3

Behrens T E J, Woolrich M W, Jenkinson M, Johansen-Berg H, Nunes R G, Clare S, Matthews P M, Brady J M and Smith S M 2003 Characterization and propagation of uncertainty in diffusion-weighted MR imaging *Magn. Reson. Med.* **50** 1077–88

Bikson M, Datta A, Rahman A and Scaturro J 2010 Electrode montages for tDCS and weak transcranial electrical stimulation: role of 'return' electrode's position and size *Clin. Neurophysiol.* **121** 1976–8

Bikson M, Dmochowski J and Rahman A 2012a The 'quasi-uniform' assumption in animal and computational models of non-invasive electrical stimulation *Brain Stimul.* **6** 704-5

Bikson M, Inoue M, Akiyama H, Deans J K, Fox J E, Miyakawa H and Jefferys J G 2004 Effects of uniform extracellular DC electric fields on excitability in rat hippocampal slices *in vitro* *J. Physiol.* **557** 175–90

Bikson M, Rahman A and Datta A 2012b Computational models of transcranial direct current stimulation *Clin. EEG Neurosci.* **43** 176–83

Bikson M, Rahman A, Datta A, Fregni F and Merabet L 2012c High-resolution modeling assisted design of customized and individualized transcranial direct current stimulation protocols *Neuromodulation* **15** 306–15

Boggio P S, Khoury L P, Martins D C, Martins O E, de Macedo E C and Fregni F 2009 Temporal cortex direct current stimulation enhances performance on a visual recognition memory task in Alzheimer disease *J. Neurol. Neurosurg. Psychiatry* **80** 444–7

Boggio P S, Nunes A, Rigonatti S P, Nitsche M A, Pascual-Leone A and Fregni F 2007 Repeated sessions of noninvasive brain DC stimulation is associated with motor function improvement in stroke patients *Restor. Neurol. Neurosci.* **25** 123–9

Borckardt J J, Bikson M, Frohman H, Reeves S T, Datta A, Bansal V, Madan A, Barth K and George M S 2012 A pilot study of the tolerability and effects of high-definition transcranial direct current stimulation (HD-tDCS) on pain perception *J. Pain* **13** 112–20

Chaturvedi A, Butson C R, Lempka S F, Cooper S E and McIntyre C C 2010 Patient-specific models of deep brain stimulation: influence of field model complexity on neural activation predictions *Brain Stimul.* **3** 65–67

Chaturvedi A, Foutz T J and McIntyre C C 2012 Current steering to activate targeted neural pathways during deep brain stimulation of the subthalamic region *Brain Stimul.* **5** 369–77

Cocosco C, Kollokian V, Kwan K and Pike G B 1997 Brainweb: Online interface to a 3D MRI simulated brain database http://brainweb.bic.mni.mcgill.ca/brainweb/

Dannhauer M, Lanfer B, Wolters C H and Knösche T R 2011 Modeling of the human skull in EEG source analysis *Hum. Brain Mapp.* **32** 1383–99

Dasilva A F, Mendonca M E, Zaghi S, Lopes M, Dossantos M F, Spierings E L, Bajwa Z, Datta A, Bikson M and Fregni F 2012 tDCS-induced analgesia and electrical fields in pain-related neural networks in chronic migraine *Headache* **52** 1283–95

Datta A 2012 Inter-individual variation during transcranial direct current stimulation and normalization of dose using MRI-derived computational models *Front. Psychiatry* **3** 91

Datta A, Baker J M, Bikson M and Fridriksson J 2011 Individualized model predicts brain current flow during transcranial direct-current stimulation treatment in responsive stroke patient *Brain Stimul.* **4** 169–74

Datta A, Bansal V, Diaz J, Patel J, Reato D and Bikson M 2009 Gyri-precise head model of transcranial DC stimulation: improved spatial focality using a ring electrode versus conventional rectangular pad *Brain Stimul.* **2** 201

Datta A, Truong D, Minhas P, Parra L C and Bikson M 2012 Inter-individual variation during transcranial direct current stimulation and normalization of dose using MRI-derived computational models *Front. Psychiatry* **3** 91

Datta A, Zhou X, Su Y, Parra L C and Bikson M 2013 Validation of finite element model of transcranial electrical stimulation using scalp potentials: implications for clinical dose *J. Neural. Eng.* **10** 036018

De Munck J 1988 The potential distribution in a layered anisotropic spheroidal volume conductor *J. Appl. Phys.* **64** 464–70

Dmochowski J P, Datta A, Bikson M, Su Y Z and Parra L C 2011 Optimized multi-electrode stimulation increases focality and intensity at target *J. Neural Eng.* **8** 046011

Edwards D, Cortes M, Datta A, Minhas P, Wassermann E M and Bikson M 2013 Physiological and modeling evidence for focal transcranial electrical brain stimulation in humans: a basis for high-definition tDCS *Neuroimage* **74** 266–75

Ferrucci R, Bortolomasi M, Vergari M, Tadini L, Salvoro B, Giacopuzzi M, Barbieri S and Priori A 2009 Transcranial direct current stimulation in severe, drug-resistant major depression *J. Affect Disord.* **118** 215–9

Ferrucci R, Mameli F, Guidi I, Mrakic-Sposta S, Vergari M, Marceglia S, Cogiamanian F, Barbieri S, Scarpini E and Priori A 2008 Transcranial direct current stimulation improves recognition memory in Alzheimer disease *Neurology* **71** 493–8

Fregni F, Freedman S and Pascual-Leone A 2007 Recent advances in the treatment of chronic pain with non-invasive brain stimulation techniques *Lancet Neurol.* **6** 188–91

Fregni F, Marcondes R, Boggio P S, Marcolin M A, Rigonatti S P, Sanchez T G, Nitsche M A and Pascual-Leone A 2006a Transient tinnitus suppression induced by repetitive transcranial magnetic stimulation and transcranial direct current stimulation *Eur. J. Neurol.* **13** 996–1001

Fregni F and Pascual-Leone A 2007 Technology insight: noninvasive brain stimulation in neurology—perspectives on the therapeutic potential of rTMS and tDCS *Nature Clin. Pract. Neurol.* **3** 383–93

Fregni F, Thome-Souza S, Nitsche M A, Freedman S D, Valente K D and Pascual-Leone A 2006b A controlled clinical trial of cathodal DC polarization in patients with refractory epilepsy *Epilepsia* **47** 335–42

Fregni F *et al* 2006c A sham-controlled, phase II trial of transcranial direct current stimulation for the treatment of central pain in traumatic spinal cord injury *Pain* **122** 197–209

Fuchs M, Wagner M and Kastner J 2007 Development of volume conductor and source models to localize epileptic foci *J. Clin. Neurophysiol.* **24** 101–19

Gabriel C, Gabriel S and Corthout E 1996a The dielectric properties of biological tissues: I. Literature survey *Phys. Med. Biol.* **41** 2231–49

Gabriel S, Lau R W and Gabriel C 1996b The dielectric properties of biological tissues: II. Measurements in the frequency range 10 Hz to 20 GHz *Phys. Med. Biol.* **41** 2251–69

Geddes L A and Baker L E 1967 The specific resistance of biological material—a compendium of data for the biomedical engineer and physiologist *Med. Biol. Eng.* **5** 271–93

Goncalve S, De Munck J, Verbunt J, Heethaar R and da Silva F 2003 *In vivo* measurement of the brain and skull resistivities using an EIT-based method and the combined analysis of SEF/SEP data *IEEE Trans. Biomed. Eng.* **50** 1124–7

Gujarati N 2003 *Basic Econometrics* (New York: McGraw-Hill)

Hagmann P, Jonasson L, Maeder P, Thiran J P, Wedeen V J and Meuli R 2006 Understanding diffusion MR imaging techniques: from scalar diffusion-weighted imaging to diffusion tensor imaging and beyond1 *Radiographics* **26** S205–23

Hallez H, Staelens S and Lemahieu I 2009 Dipole estimation errors due to not incorporating anisotropic conductivities in realistic head models for EEG source analysis *Phys. Med. Biol.* **54** 6079–93

Hallez H, Vanrumste B, Hese P, Delputte S and Lemahieu I 2008 Dipole estimation errors due to differences in modeling anisotropic conductivities in realistic head models for EEG source analysis *Phys. Med. Biol.* **53** 1877–94

Holdefer R N, Sadleir R and Russell M J 2006 Predicted current densities in the brain during transcranial electrical stimulation *Clin. Neurophysiol.* **117** 1388–97

Hyun Sang S, Sang Hyuk K, Won Hee L and Tae-Seong K 2009 Realistic simulation of transcranial direct current stimulation via 3-d high-resolution finite element analysis: effect of tissue anisotropy *EMBC'09: Annu. Int. Conf. IEEE Engineering in Medicine and Biology Society* pp 638–41

Hyun Sang S, Won Hee L, Young Sun C, Ji-Hwan K and Tae-Seong K 2010 Reduced spatial focality of electrical field in tDCS with ring electrodes due to tissue anisotropy *EMBC'10: Annu. Int. Conf. of the IEEE Engineering in Medicine and Biology Society* pp 2053–6

Jiang H, van Zijl P C, Kim J, Pearlson G D and Mori S 2006 DtiStudio: resource program for diffusion tensor computation and fiber bundle tracking *Comput. Methods Programs Biomed.* **81** 106–16

Jones D, Horsfield M and Simmons A 1999 Optimal strategies for measuring diffusion in anisotropic systems by magnetic resonance imaging *Magn. Reson. Med.* **42** 512–25

Kabakov A Y, Muller P A, Pascual-Leone A, Jensen F E and Rotenberg A 2012 Contribution of axonal orientation to pathway-dependent modulation of excitatory transmission by direct current stimulation in isolated rat hippocampus *J. Neurophysiol.* **107** 1881–9

Kim S, Kim T, Zhou Y and Singh M 2001 Influence of conductivity tensors in the finite element model of the head on the forward solution of EEG *IEEE Nucl. Sci. Symp. Conf. Rec.* pp 1892–6

Kun W, Shanan Z, Mueller B A, Lim K O, Zhongming L and Bin H 2008 A new method to derive white matter conductivity from diffusion tensor MRI *IEEE Trans. Biomed. Eng.* **55** 2481–6

Kybic J, Clerc M, Abboud T, Faugeras O, Keriven R and Papadopoulo T 2005 A common formalism for the integral formulations of the forward EEG problem *IEEE Trans. Med. Imaging* **24** 12–28

Lazar M and Alexander A L 2003 An error analysis of white matter tractography methods: synthetic diffusion tensor field simulations *NeuroImage* **20** 1140–53

Le Bihan D, Mangin J F, Poupon C, Clark C A, Pappata S, Molko N and Chabriat H 2001 Diffusion tensor imaging: concepts and applications *J. Magn. Reson. Imaging* **13** 534–46

Lee W, Seo H, Kim S, Cho M, Lee S and Kim T 2009 Influence of white matter anisotropy on the effects of transcranial direct current stimulation: a finite element study *13th Int. Conf. on Biomedical Engineering* pp 460–4

Leemans A and Jones D K 2009 The *B*-matrix must be rotated when correcting for subject motion in DTI data *Mag. Reson. Med.* **61** 1336–49

Lujan J L, Chaturvedi A, Malone D A, Rezai A R, Machado A G and McIntyre C C 2012 Axonal pathways linked to therapeutic and nontherapeutic outcomes during psychiatric deep brain stimulation *Hum. Brain Mapp.* **33** 958–68

Lujan J L, Chaturvedi A and McIntyre C C 2008 Tracking the mechanisms of deep brain stimulation for neuropsychiatric disorders *Front. Biosci.* **13** 5892–904

Malmivuo J and Plonsey R 1995 *Bioelectromagnetism: Principles and Applications of Bioelectric and Biomagnetic Fields* (Oxford: Oxford University Press)

Marin G, Guerin C, Baillet S, Garnero L and Meunier G 1998 Influence of skull anisotropy for the forward and inverse problem in EEG: simulation studies using FEM on realistic head models *Hum. Brain Mapp.* **6** 250–69

Meijs J, Weier O, Peters M and Van Oosterom A 2002 On the numerical accuracy of the boundary element method (EEG application) *IEEE Trans. Biomed. Eng.* **36** 1038–49

Mignon A, Laudenbach V, Guischard F, Limoge A, Desmonts J M and Mantz J 1996 Transcutaneous cranial electrical stimulation (Limoge's currents) decreases early buprenorphine analgesic requirements after abdominal surgery *Anesth. Analg.* **83** 771–5

Minhas P, Bansal V, Patel J, Ho J S, Diaz J, Datta A and Bikson M 2010 Electrodes for high-definition transcutaneous DC stimulation for applications in drug delivery and electrotherapy, including tDCS *J. Neurosci. Methods* **190** 188–97

Miranda P C, Correia L, Salvador R and Basser P J 2007 Tissue heterogeneity as a mechanism for localized neural stimulation by applied electric fields *Phys. Med. Biol.* **52** 5603–17

Miranda P C, Pajevic S, Pierpoali C, Hallett M and Basser P 2001 The distribution of currents induced in the brain by magnetic stimulation: a finite element analysis incorporating DT-MRI-derived conductivity data *Proc. Int. Society for Magnetic Resonance in Medicine* p 1540

Munck J and Peters M 1993 A fast method to compute the potential in the multi-sphere model *IEEE Trans. Biomed. Eng.* **40** 1166–74

Nicholson P W 1965 Specific impedance of cerebral white matter *Exp. Neurol.* **13** 386–401

Nitsche M A, Boggio P S, Fregni F and Pascual-Leone A 2009 Treatment of depression with transcranial direct current stimulation (tDCS): a review *Exp. Neurol.* **219** 14–19

Nunez P L and Srinivasan R 2006 *Electric Fields of the Brain: the Neurophysics of EEG* (Oxford: Oxford University Press)

Oostendorp T, Delbeke J and Stegeman D 2002 The conductivity of the human skull: results of *in vivo* and *in vitro* measurements *IEEE Trans. Biomed. Eng.* **47** 1487–92

Oostendorp T F, Hengeveld Y A, Wolters C H, Stinstra J, van Elswijk G and Stegeman D F 2008 Modeling transcranial DC stimulation *EMBS'08: 30th Annu. Int. Conf. of the IEEE Engineering in Medicine and Biology Society* pp 4226–9

Opitz A, Legon W, Rowlands A, Bickel W K, Paulus W and Tyler W J 2013 Physiological observations validate finite element models for estimating subject-specific electric field distributions induced by transcranial magnetic stimulation of the human motor cortex *NeuroImage* **81** 253–64

Parazzini M, Fiocchi S and Ravazzani P 2012a Electric field and current density distribution in an anatomical head model during transcranial direct current stimulation for tinnitus treatment *Bioelectromagnetics* **33** 476–87

Parazzini M, Fiocchi S, Rossi E, Paglialonga A and Ravazzani P 2011 Transcranial direct current stimulation: estimation of the electric field and of the current density in an anatomical human head model *IEEE Trans. Biomed. Eng.* **58** 1773–80

Parazzini M, Rossi E, Fiocchi S, Liorni I, Rossi L, Priori A and Ravazzani P 2012b Role of human variability on the estimation of the electric field and of the current density during transcranial direct current stimulation *EMC EUROPE: Int. Symp. on Electromagnetic Compatibility* pp 1–4

Plis S M, George J S, Jun S C, Ranken D M, Volegov P L and Schmidt D M 2007 Probabilistic forward model for electroencephalography source analysis *Phys. Med. Biol.* **52** 5309

Plonsey R and Heppner D B 1967 Considerations of quasistationaryity in electrophysiological systems *Bull. Math. Biophys.* **29** 657–64

Polania R, Paulus W and Nitsche M A 2012 Modulating cortico-striatal and thalamo-cortical functional connectivity with transcranial direct current stimulation *Hum. Brain Mapp.* **33** 2499–508

Radman T, Ramos R L, Brumberg J C and Bikson M 2009 Role of cortical cell type and morphology in sub-and suprathreshold uniform electric field stimulation *Brain Stimul.* **2** 215

Rampersad S M, Stegeman D F and Oostendorp T F 2013 Single-layer skull approximations perform well in transcranial direct current stimulation modeling *IEEE Trans. Neural. Syst. Rehabil. Eng.* **21** 346–53

Rullmann M, Anwander A, Dannhauer M, Warfield S K, Duffy F H and Wolters C H 2009 EEG source analysis of epileptiform activity using a 1 mm anisotropic hexahedra finite element head model *NeuroImage* **44** 399–410

Rush S and Driscoll D A 1968 Current distribution in the brain from surface electrodes *Anesth. Analg.* **47** 717–23

Ruthotto L, Kugel H, Olesch J, Fischer B, Modersitzki J, Burger M and Wolters C H 2012 Diffeomorphic susceptibility artifact correction of diffusion-weighted magnetic resonance images *Phys. Med. Biol.* **57** 5715–31

Sadleir R and Argibay A 2007 Modeling skull electrical properties *Ann. Biomed. Eng.* **35** 1699–712

Salvador R, Silva S, Basser P and Miranda P 2011 Determining which mechanisms lead to activation in the motor cortex: a modeling study of transcranial magnetic stimulation using realistic stimulus waveforms and sulcal geometry *Clin. Neurophysiol.* **122** 748–58

Schlaug G, Renga V and Nair D 2008 Transcranial direct current stimulation in stroke recovery *Arch. Neurol.* **65** 1571–6

Shahid S and Wen P 2010 Analytic and numeric evaluation of EEG forward problem using spherical volume conductor models *IEEE Int. Conf. on Complex Medical Engineering* pp 28–33

Shahid S, Wen P and Ahfock T 2012 Effects of model complexity and tissue anisotropic conductivity on cortical modulation during transcranial direct current stimulation *IET Sci. Meas. Technol.* **6** 464–73

Shahid S, Wen P and Ahfock T 2013 Numerical investigation of white matter anisotropic conductivity in defining current distribution under tDCS *Comput. Methods Programs Biomed.* **109** 48–64

Shahid S, Wen P and Ahfock T 2014 Assessment of electric field distribution in anisotropic cortical and subcortical regions under the influence of tDCS *Bioelectromagnetics* **35** 41–57

Shimony J S, McKinstry R C, Akbudak E, Aronovitz J A, Snyder A Z, Lori N F, Cull T S and Conturo T E 1999 Quantitative diffusion-tensor anisotropy brain MR imaging: normative human data and anatomic analysis *Radiology* **212** 770–84

Silva S, Basser P J and Miranda P C 2008 Elucidating the mechanisms and loci of neuronal excitation by transcranial magnetic stimulation using a finite element model of a cortical sulcus *Clin. Neurophysiol.* **119** 2405–13

Squillacote A H 2007 The ParaView guide: a parallel visualization application *Kitware*

Suh H S, Lee W H and Kim T S 2012 Influence of anisotropic conductivity in the skull and white matter on transcranial direct current stimulation via an anatomically realistic finite element head model *Phys. Med. Biol.* **57** 6961–80

Tensaouti F, Lotterie J A and Berry I 2009 Fiber tracking on the phantom dataset by using Sisyphe software *MICCAI Workshop on Diffusion Modelling and the Fiber Cup (DMFC'09) (London, UK)*

Tuch D S 2004 Q-ball imaging *Magn. Reson. Med.* **52** 1358–72

Tuch D S, Reese T G, Wiegell M R, Makris N, Belliveau J W and Wedeen V J 2002 High angular resolution diffusion imaging reveals intravoxel white matter fiber heterogeneity *Magn. Reson. Med.* **48** 577–82

Tuch D S, Wedeen V J, Dale A M, George J S and Belliveau J W 1999 Conductivity mapping of biological tissue using diffusion MRI *Int. Symp. on Occupational Electrical Injury* vol 888 pp 314–6

Vanneste S, Plazier M, Ost J, van der Loo E, Van de Heyning P and De Ridder D 2010 Bilateral dorsolateral prefrontal cortex modulation for tinnitus by transcranial direct current stimulation: a preliminary clinical study *Exp. Brain Res.* **202** 779–85

Wakana S *et al* 2007 Reproducibility of quantitative tractography methods applied to cerebral white matter *NeuroImage* **36** 630–44

Wang L, Zhong X, Zhang L, Tiwari D and Mao H 2010 Ultra-short TE (UTE) imaging of skull and a quantitative comparison of skull images obtained from MRI and CT *ISMRM-ESMRMB Joint Annu. Meeting (Stockholm, Sweden)* p 796

Wang Y, Haynor D R and Kim Y 2001 An investigation of the importance of myocardial anisotropy in finite-element modeling of the heart: methodology and application to the estimation of defibrillation efficacy *IEEE Trans. Biomed. Eng.* **48** 1377–89

Webster B R, Celnik P A and Cohen LG 2006 Noninvasive brain stimulation in stroke rehabilitation *NeuroRx* **3** 474–81

Wedeen V J, Wang R P, Schmahmann J D, Benner T, Tseng W Y I, Dai G, Pandya D N, Hagmann P, D'Arceuil H and de Crespigny A J 2008 Diffusion spectrum magnetic resonance imaging (DSI) tractography of crossing fibers *NeuroImage* **41** 1267–77

Williams J A, Imamura M and Fregni F 2009 Updates on the use of non-invasive brain stimulation in physical and rehabilitation medicine *J. Rehabil. Med.* **41** 305–11

Wolters C 2003 Influence of tissue conductivity inhomogeneity and anisotropy on EEG/MEG based source localization in the human brain *PhD Thesis* MPI for Human Cognitive and Brain Sciences/MPI of Cognitive Neuroscience, Leipzig

Wolters C H, Anwander A, Tricoche X, Weinstein D, Koch M A and MacLeod R S 2006 Influence of tissue conductivity anisotropy on EEG/MEG field and return current computation in a realistic head model: a simulation and visualization study using high-resolution finite element modeling *NeuroImage* **30** 813–26

Yeh F C and Tseng W Y I 2011 NTU-90: A high angular resolution brain atlas constructed by q-space diffeomorphic reconstruction *NeuroImage* **58** 91–99

Zheng X, Alsop D C and Schlaug G 2011 Effects of transcranial direct current stimulation (tDCS) on human regional cerebral blood flow *NeuroImage* **58** 26–33